

RESEARCH ARTICLE | APRIL 20 2023

GaSb band-structure models for electron density determinations from Raman measurements

Maicol A. Ochoa  ; James E. Maslar ; Herbert S. Bennett

 Check for updates

Journal of Applied Physics 133, 155702 (2023)

<https://doi.org/10.1063/5.0140357>


View
Online


Export
Citation

CrossMark



Time to get excited.
Lock-in Amplifiers – from DC to 8.5 GHz

[Find out more](#)

 Zurich
Instruments

GaSb band-structure models for electron density determinations from Raman measurements

Cite as: J. Appl. Phys. **133**, 155702 (2023); doi: [10.1063/5.0140357](https://doi.org/10.1063/5.0140357)

Submitted: 28 December 2022 · Accepted: 2 April 2023 ·

Published Online: 20 April 2023



Maicol A. Ochoa,^{1,2,a)} James E. Maslar,¹ and Herbert S. Bennett^{1,3}

AFFILIATIONS

¹National Institute of Standards and Technology, Gaithersburg, Maryland 20899, USA

²Department of Chemistry and Biochemistry, University of Maryland, College Park, Maryland 20742, USA

³AltaTech Strategies LLC, Kensington, Maryland 20891, USA

Note: This paper is part of the Special Topic on Semiconductor Physics: Plasma, Thermal, Elastic, and Acoustic Phenomena.

a) Author to whom correspondence should be addressed: maicol@nist.gov

ABSTRACT

We investigate the use of Raman spectroscopy to measure carrier concentrations in *n*-type GaSb epilayers to aid in the development of this technique for the nondestructive characterization of transport properties in doped semiconductors. The carrier concentration is quantified by modeling the measured coupled optical phonon-free carrier plasmon mode spectra. We employ the Lindhard–Mermin optical susceptibility model with contributions from carriers in the two lowest GaSb conduction-band minima, the Γ and *L* minima. Furthermore, we evaluate three conduction-band models: (1) both minima parabolic and isotropic, (2) the Γ minimum non-parabolic and isotropic and the *L* minima parabolic and isotropic, and (3) the Γ minimum non-parabolic and isotropic and the *L* minima parabolic and ellipsoidal. For a given epilayer, the carrier concentration determined from the spectral simulations was consistently higher for the ellipsoidal *L* minima model than the other two models. To evaluate the conduction-band models, we calculated the *L* to Γ electron mobility ratio necessary for the electron concentrations from the Raman spectral measurements to reproduce those from the Hall effect measurements. We found that the model with the ellipsoidal *L* minima agreed best with reported carrier-dependent mobility-ratio values. Hence, employing isotropic *L* minima in GaSb conduction-band models, a common assumption when describing the GaSb conduction band, likely results in an underestimation of carrier concentration at room temperature and higher doping levels. This observation could have implications for Raman spectral modeling and any investigation involving the GaSb conduction band, e.g., modeling electrical measurements or calculating electron mobility.

Published under an exclusive license by AIP Publishing. <https://doi.org/10.1063/5.0140357>

I. INTRODUCTION

GaSb and related alloy semiconductors have numerous current and potential applications, including mid-infrared sources^{1–5} and detectors^{6–8} and high-speed, low-power electronic devices.^{9–11} Growth of these devices on native GaSb substrates is generally preferred. However, interest is increasing in growing these devices heteroepitaxially on silicon or gallium arsenide substrates.^{5,12–14} This interest is due to many factors. For example, silicon and gallium arsenide substrates are more cost effective and exhibit better thermal properties compared to GaSb substrates. In addition, the use of silicon substrates can facilitate the incorporation of GaSb-based devices into photonic integrated circuits.^{5,13,14} The lattice mismatch between GaSb and GaAs and silicon substrates and the polarity mismatch and difference in thermal expansion between GaSb and

silicon substrates generally result in the creation of lattice defects, which can limit device performance if the defects propagate to the device layers. To reduce defect formation in the device layers, various types of buffer layers are utilized between the device layers and the substrate.^{5,12–14} Some of these buffer layers can be electrically active. This precludes unambiguous characterization of transport properties of the GaSb and GaSb-based layers in the device using frequently employed single magnetic field Hall effect measurements since more than one carrier type contributes to sample conductivity and Hall coefficient.¹⁵ As an understanding of the transport properties in GaSb and GaSb-based materials is fundamental to the design and optimization of devices based on these materials, development of alternative techniques that can selectively characterize transport properties of specific (sometimes buried) layers in device structures is desirable.

Raman spectroscopy provides a non-contact, non-destructive, and spatially resolved method for characterizing buried layers.^{16,17} Furthermore, Raman spectroscopy has been employed to investigate carrier properties in many compound semiconductor materials. Such an analysis involves observation of the coupled phonon–plasmon modes, which result from the interaction between the polar longitudinal optical (LO) phonon mode and the collective carrier plasmon mode.¹⁸ Quantitative analysis requires knowledge of the relationship between the coupled phonon–plasmon mode frequency and the free carrier concentration. Many investigations have focused on coupled mode spectra in *n*-type GaAs or InP.^{16,18–26} For such materials, the electron population generally is significant in only a single spherical energy band minimum, the Γ minimum, at typical experimental conditions. Hence, the plasmon can be described in terms of a single, isotropic electron effective mass. In contrast, for GaSb and related alloys, the electron population can be significant in two energy band minima, the Γ and *L* minima, at typical experimental conditions. Furthermore, the *L* minima are ellipsoidal. Hence, the plasmon is best described in terms of two electron effective masses, one isotropic and one anisotropic. The quantitative analysis of the coupled mode spectra in antimonide-based materials has been described for *n*-type GaSb^{27,28} and GaInAsSb.^{28–30} In the GaSb studies, the coupled mode spectra were simulated using electric susceptibility described in terms of different classical models. However, it has been shown that a more accurate determination of carrier concentration in III–V semiconductors can be obtained when using a Lindhard–Mermin (LM) model for the electric susceptibility.^{31–33}

In this report, we analyze the *n*-type GaSb coupled phonon–plasmon mode spectra first presented in Ref. 27 using an LM model, rather than the classical model originally employed. Furthermore, considering the complexity of the GaSb conduction-band structure,^{34–43} we compare the following three conduction-band models to evaluate the impact of model parameters on fit results:

- (1) (*P–P*) model. A parabolic Γ minimum with an isotropic effective mass and a parabolic *L* minimum with an isotropic effective mass described by the geometric mean of the longitudinal and transverse effective masses.
- (2) (*NP–P*) model. A structure as with the (*P–P*) model except that we employ a non-parabolic Γ minimum.
- (3) (*NP–E*) model. A structure as with the (*NP–P*) model except that we employ a non-isotropic, ellipsoidal *L* minimum.

The organization of the paper is as follows. In Sec. II, we describe the experimental Hall and Raman measurements. In Sec. III, we introduce the mathematical model for the GaSb Raman line shape, optical susceptibility, electronic structure, and electron density. In Sec. IV, utilizing the foregoing three models, we calculate the resulting electron densities extracted from Raman measurements and then compare the results with those obtained from Hall measurements. In Sec. V, we summarize our findings.

II. EXPERIMENTAL RAMAN MEASUREMENTS IN GaSb

The deposition and characterization of the six *n*-type doped GaSb epilayers listed in Table I have been described previously.²⁷ The epilayers were deposited on semi-insulating GaAs substrates

TABLE I. Selected details concerning the epilayers examined in this work.

Epilayer	DETe mole fraction ($\times 10^{-9}$)	$n_{\text{Hall}}^a (\times 10^{18})$ (cm^{-3})	μ_{Hall}^b ($\times 10^3 \text{ cm}^2/\text{V s}$)
1	5.0	0.49	3.18
2	7.5	0.65	2.74
3	10	0.74	2.53
4	15	0.88	2.26
5	25	1.04	1.93
6	50	1.17	1.65

^aThe authors estimate that the statistical variation for n_{Hall} is $\pm 10\%$ based on measurement reproducibility.

^bThe authors estimate that the statistical variation for μ_{Hall} is $\pm 10\%$ based on measurement reproducibility.

using organometallic vapor phase epitaxy and doped with tellurium using diethyltellurium (DETe) at the mole fractions in the reactor given in Table I.^{44,45} All epilayers were nominally $2.5 \mu\text{m}$ thick; however, the three band models presented in Sec. III are valid for all thicknesses and are not specific to Raman spectral measurements of *n*-type GaSb. GaSb epilayers grown without DETe flow were unintentionally doped *p*-type due to native defects with a 300 K hole concentration and mobility of $1.44 \times 10^{16} \text{ cm}^{-3}$ and $804 \text{ cm}^2/\text{V s}$, respectively, and a 77 K hole concentration and mobility of $4.08 \times 10^{15} \text{ cm}^{-3}$ and $4821 \text{ cm}^2/\text{V s}$, respectively. These values correspond to a native acceptor concentration of $\approx 8.8 \times 10^{15} \text{ cm}^{-3}$, assuming a doubly ionizable defect⁴⁶ with energy levels⁴⁷ of 0.03 and 0.1 eV and a negligible native donor concentration. Because the total electron concentration in the most lightly Te-doped epilayer (epilayer 1) was $1.33 \times 10^{18} \text{ cm}^{-3}$ at 300 K, we ignore in this work compensation.

We performed the Raman measurements with 752.22 nm radiation from a krypton ion laser at room temperature in a back-scattering geometry described by $z(x, y)\bar{z}$, where x, y, z , and \bar{z} denote the [100], [010], [001], and [00 $\bar{1}$] directions, respectively, as described previously.⁴⁸ The laser power density at the sample was less than $\approx 9 \text{ W}/\text{cm}^2$. Collected radiation was coupled into a single grating, 0.46 m focal length, $f/5.3$ imaging spectrograph operating with a 1200 grooves per millimeter holographic grating (750 nm blaze wavelength) and 130 mm slits. A thermo-electrically cooled (to 90°C), 1024×128 pixel array ($26 \mu\text{m} \times 26 \mu\text{m}$ square pixels), deep depletion back-illuminated charge coupled device camera system was employed. The instrumental bandpass (FWHM) was $\approx 2.9 \text{ cm}^{-1}$. All spectra shown represent the average of two spectra, each of which was obtained with 300 s integration time. Spectrograph wavelength calibration was performed with atomic lines from an uranium hollow cathode tube. All Raman scattering intensities were corrected for the wavelength-dependent response of the optical system using a white-light source of known relative irradiance.⁴⁸ Only the coupled mode spectra are shown in this report. These spectra were obtained by removing the LO phonon scattering, the second order phonon scattering, and the nitrogen and oxygen molecular Raman scattering from ambient air, and a cubic polynomial baseline from the original spectra, as described in Appendix A.

Electron concentration and mobility were determined using single magnetic field Hall effect measurements based on the van der Pauw method. Ohmic contacts were made to GaSb using an indium metal. Measurements were performed at room temperature using a 1 T magnetic field. These data are listed in Table I.

III. THEORY

Using the three conduction band-structure models presented in Sec. I, we describe now how to obtain the electron concentrations numerically on a given GaSb epilayer from the Raman measurements.

A. The Raman line shape

The Raman line shape $L(q, \omega)$ at an angular frequency ω , scattering wavevector q , and temperature T is given by the full longitudinal dielectric response function $\epsilon(q, \omega)$ ^{18,49}

$$L(q, \omega) = \frac{1}{1 - e^{-\beta\hbar\omega}} \left(\frac{\omega_o^2 - \omega^2}{\omega_{TO}^2 - \omega^2} \right) \text{Im} \left(-\frac{1}{\epsilon(q, \omega)} \right). \quad (1)$$

In the above expression, $\beta = 1/k_B T$, where k_B is the Boltzmann constant, ω_{LO} and ω_{TO} are the longitudinal (LO) and transverse (TO) phonon angular frequencies, $\omega_o = \omega_{TO} \sqrt{1 + C_{FH}}$, and C_{FH} is the dimensionless Faust–Henry coefficient. The dielectric response function $\epsilon(q, \omega)$ has contributions from the valence and conduction electrons, the polar lattice phonons, and their coupling. Explicitly,

$$\epsilon(q, \omega) = 1 + 4\pi\chi_{VE} + 4\pi\chi_{pho}(\omega) + 4\pi\chi_e^{GaSb}(q, \omega), \quad (2)$$

where χ_{VE} is the dielectric term due to the valence electrons, and $\chi_{pho}(\omega)$ is the contribution originating in the polar lattice phonons,

$$4\pi\chi_{pho}(\omega) = \epsilon_\infty \left(\frac{\omega_{LO}^2 - \omega_{TO}^2}{\omega_{TO}^2 - \omega^2} \right), \quad (3)$$

with $\epsilon_\infty = 1 + 4\pi\chi_{VE}$. In Eq. (3), we neglect the phonon damping.

The term χ_e^{GaSb} in Eq. (2) accounts for the conduction-band electron contribution to the GaSb optical response and the Raman spectrum and depends on the band-structure model. We assume that the electrons in the Γ and L bands contribute independently to χ_e^{GaSb} , and since the L band has four equivalent minima in the first Brillouin zone, we write

$$\chi_e^{GaSb}(\omega, q) = \chi_\Gamma(\omega, q) + \frac{1}{2} \sum_{i=1}^8 \chi_L^{(i)}(\omega, q), \quad (4)$$

where the terms χ_Γ and χ_L depend on the corresponding dispersion relations E_Γ and E_L according to the Lindhard form

$$\chi_i(\omega, q) = \frac{e^2}{4\pi^3 q^2} \int dk^3 \frac{f(E_i(k), E_F)}{\hbar(\omega + i\gamma_i) + E_i(k) - E_i(k+q)} - \frac{f(E_i(k), E_F)}{\hbar(\omega + i\gamma_i) + E_i(k-q) - E_i(k)} \quad (5)$$

TABLE II. Parameter values used in the calculation of the GaSb band structure and susceptibility. These values are derived from other parameters in the literature as described in Appendix B, unless a reference is given. m_o is the electron mass.

Band-structure parameters		Susceptibility parameters	
m_Γ	$0.035 m_o$	ω_{LO}	236 cm^{-1}
$m_{\Gamma L}^a$	$1.4 m_o$	ω_{TO}	226 cm^{-1}
m_{iL}	$0.081 m_o$	ϵ_∞^b	14.4
ζ^c	-0.84	C_{FH}	-0.245
$E_{\Gamma 0}$	0.727 eV	a_L^d	$6.09 \times 10^{-10} \text{ m}$
$E_{L0} - E_{\Gamma 0}$	0.0847 eV	q^e	$7.422 \times 10^5 \text{ cm}^{-1}$

^aReference 51.

^bReference 53.

^cReference 52.

^dReference 47.

^eReference 54.

for $i = \Gamma, L$. In Eq. (5), $f(E(k), E_F) = (1 + \exp(\beta(E(k) - E_F)))^{-1}$ is the Fermi function and E_F is the Fermi energy. Following Mermin,⁵⁰ to properly account for the effects of damping, we modify $\chi_i(\omega, q)$ as follows:

$$\chi_i(\omega, q) \rightarrow \frac{\omega + i\gamma_i}{\omega} \chi_i(\omega, q) \left(\frac{1}{1 + i\gamma_i \chi_i(\omega, q) / \chi_i(0, q)} \right). \quad (6)$$

In this form, the Raman line shape in Eq. (1) depends parameterically on the Fermi energy and the damping rates γ_Γ and γ_L . Thus, after implementing the above expressions numerically adopting one of the three band-structure models (see below Subsections III C–III E) and varying E_F , γ_Γ , and γ_L , we fit the calculated Raman line shapes to the experimental line shapes. Table II lists the values of the input parameters.

B. Electron density

The Γ and L electron densities depend on the density of states (DOS) $\rho(\epsilon)$, E_F , and the Fermi function $f(\epsilon, E_F) = (1 + \exp(\beta(\epsilon - E_F)))^{-1}$,

$$n_i(E_F) = \int d\epsilon \rho_i(\epsilon) f(\epsilon, E_F) \quad (i = \Gamma, L), \quad (7)$$

where the DOS is a function of the dispersion relation $E_i(k)$,

$$\rho_i(\epsilon) = \int \frac{d^3k}{(2\pi)^3} \delta(\epsilon - E_i(k)) \quad (i = \Gamma, L). \quad (8)$$

In Eq. (7), integrals are evaluated from the bottoms of the respective Γ and L bands and in Eq. (8) from the $k = k_o$ to the edge of the first Brillouin zone. This implies that the electron densities depend only on the Γ to L energy difference and not on the values of $E_{\Gamma 0}$ and E_{L0} . Moreover, the electron densities are sensitive to the band-structure model, represented by $E_i(k)$. The total electron density n_{tot} is the sum of the electron densities in the Γ -band n_Γ and each of the four L band minima $n_L^{(k)}$.

Downloaded from http://pubs.aip.org/jap/article-pdf/doi/10.1063/1.50140357/16883988/155702_1_5.0140357.pdf

C. (P-P) model

For this model, we assume that the dispersion relations for the Γ and L bands are parabolic near their corresponding minima,

$$E_{\Gamma}(k) = E_{\Gamma 0} + \frac{(\hbar k)^2}{2m_{\Gamma}}, \quad (9)$$

$$E_L(k) = E_{L0} + \frac{(\hbar k)^2}{2m_L}, \quad (10)$$

where $E_{\Gamma 0}$ and E_{L0} are the energy value at the bottom of the Γ and L -band, m_{Γ} is the Γ -band effective mass, $m_L = (m_{Lx}m_{Ly}^2)^{1/3}$, and m_{Lx} and m_{Ly} are the transverse and longitudinal effective masses in Table II. The corresponding DOSs are

$$\rho_{\Gamma}(\varepsilon) = \frac{1}{4\pi^2} \frac{(2m_{\Gamma})^{3/2}}{\hbar^3} \sqrt{\varepsilon - E_{\Gamma 0}}, \quad (11)$$

$$\rho_L(\varepsilon) = \frac{1}{4\pi^2} \frac{(2m_L)^{3/2}}{\hbar^3} \sqrt{\varepsilon - E_{L0}}. \quad (12)$$

Table II lists the values of the band structure used in our calculations.

D. (NP-P) model

In this model, we assume that the Γ -band dispersion relation is isotropically nonparabolic,

$$E_{\Gamma}(k) = E_{\Gamma 0} + \frac{(\hbar k)^2}{2m_{\Gamma}} + \left(\frac{\zeta}{E_{\Gamma 0}}\right) \left(\frac{(\hbar k)^2}{2m_{\Gamma}}\right)^2, \quad (13)$$

where ζ is the non-parabolicity coefficient in Table II. For the L -band, this model assumes that E_L is parabolic as in Eq. (10). The nonparabolic Γ -band DOS is (see Appendix C)

$$\rho_{\Gamma}(\varepsilon) = \frac{(2m_{\Gamma})^{3/2}}{4\pi^2 \hbar^3} \frac{\sqrt{1 - \sqrt{1 + 4(\zeta/E_{\Gamma 0})(\varepsilon - E_{\Gamma 0})}}}{\sqrt{-2(\zeta/E_{\Gamma 0})\sqrt{1 + 4(\zeta/E_{\Gamma 0})(\varepsilon - E_{\Gamma 0})}}}. \quad (14)$$

We note that $\rho_{\Gamma}(\varepsilon)$ in Eq. (14) converges to the parabolic limit, Eq. (11) for vanishing ζ . Finally, the L -band DOS is the same as in the (P-P) model, Eq. (12).

E. (NP-E) model

This model takes into account that the energy dispersion near each GaSb L -conduction-band minimum is an ellipsoid characterized by m_{Lx} and m_{Ly} ,

$$E_L(k) = E_{L0} + \frac{(\hbar k_z)^2}{2m_{Lz}} + \frac{\hbar^2}{2m_{Lx}}(k_x^2 + k_y^2). \quad (15)$$

For the (NP-E) model, we find the L -band DOS by integrating Eq. (8) in ellipsoidal coordinates after substituting $E_L(k)$ [Eq. (15)] (see Appendix D for details). The resulting expression for the

L -band DOS is

$$\rho_L(\varepsilon) = \frac{a^3}{8\pi^2} \int_0^{\pi} dv \frac{\left(\frac{A(\varepsilon, v)}{aB(\varepsilon, v)} - 1\right)}{B(\varepsilon, v) \sqrt{aA(\varepsilon, v)/B(\varepsilon, v)}} \sin v + \frac{a^3}{8\pi^2} \int_0^{\pi} dv \frac{1}{B(\varepsilon, v) \sqrt{aA(\varepsilon, v)/B(\varepsilon, v)}} \sin^3 v, \quad (16)$$

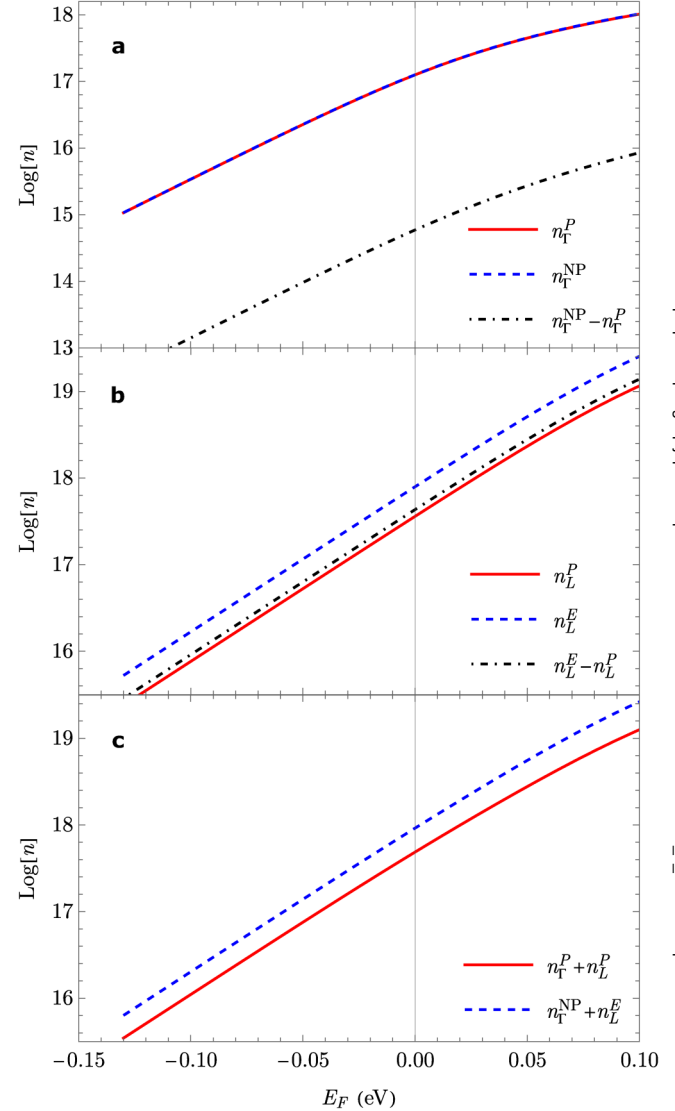


FIG. 1. The log of the GaSb electron density as a function of E_F at 300 K. (a) Γ -band electron density n_{Γ} for a model with parabolic (P) and nonparabolic (NP) dispersion relations. (b) L -band electron density n_L for a model with parabolic (P) and ellipsoidal (E) dispersion relations. (c) Total electron density ($n_{\Gamma} + n_L$) for the fully parabolic model and the model with nonparabolic (NP) Γ and ellipsoidal (E) L bands. Table II includes the parameters used here.

Downloaded from http://pubs.aip.org/jap/article-pdf/doi/10.1063/5.0140357/16883988/155702_1_5.0140357.pdf

given in terms of the functions

$$A(\varepsilon, \nu) = \varepsilon - E_{L0} + \frac{\hbar^2 a^2 \sin^2 \nu}{2m_{IL}}, \quad (17)$$

$$B(\varepsilon, \nu) = \frac{\hbar^2 a}{2} \left(\frac{\cos^2 \nu}{m_{IL}} + \frac{\sin^2 \nu}{m_{IL}} \right), \quad (18)$$

$$a = \frac{2(E_L(k) - E_{L0})\sqrt{m_{IL}^2 - m_{IL}^2}}{\hbar^2}. \quad (19)$$

For the Γ band, this model assumes the nonparabolic forms for the dispersion relation and the DOS in Eqs. (13) and (14).

We stress that in the case of the (P-P) and (NP-P) models, we approximate $\rho_L(\varepsilon)$ by the form in Eq. (12) with effective mass

$m_L = (m_{IL}^2 m_{LL})^{1/3}$. The latter form for the effective mass results from a low-temperature approximation to the electron density⁵⁵ consisting of replacing the Fermi function by the exponential $\exp\{-\beta(E - E_F)\}$ in Eq. (7).

IV. DISCUSSION

Starting from the GaSb band structure, we investigate the implications of these models for interpreting Raman measurements. First, we analyze the electron density as a function of Fermi energy for each model in Fig. 1, for which the Fermi energies are referenced to the bottom of the conduction band at the Γ symmetry point. We note that corrections to the Γ -band electron density due to the nonparabolicity near the conduction-band minimum affect this value by less than 1% as compared with the estimation made by the parabolic approximation. On the contrary, accounting

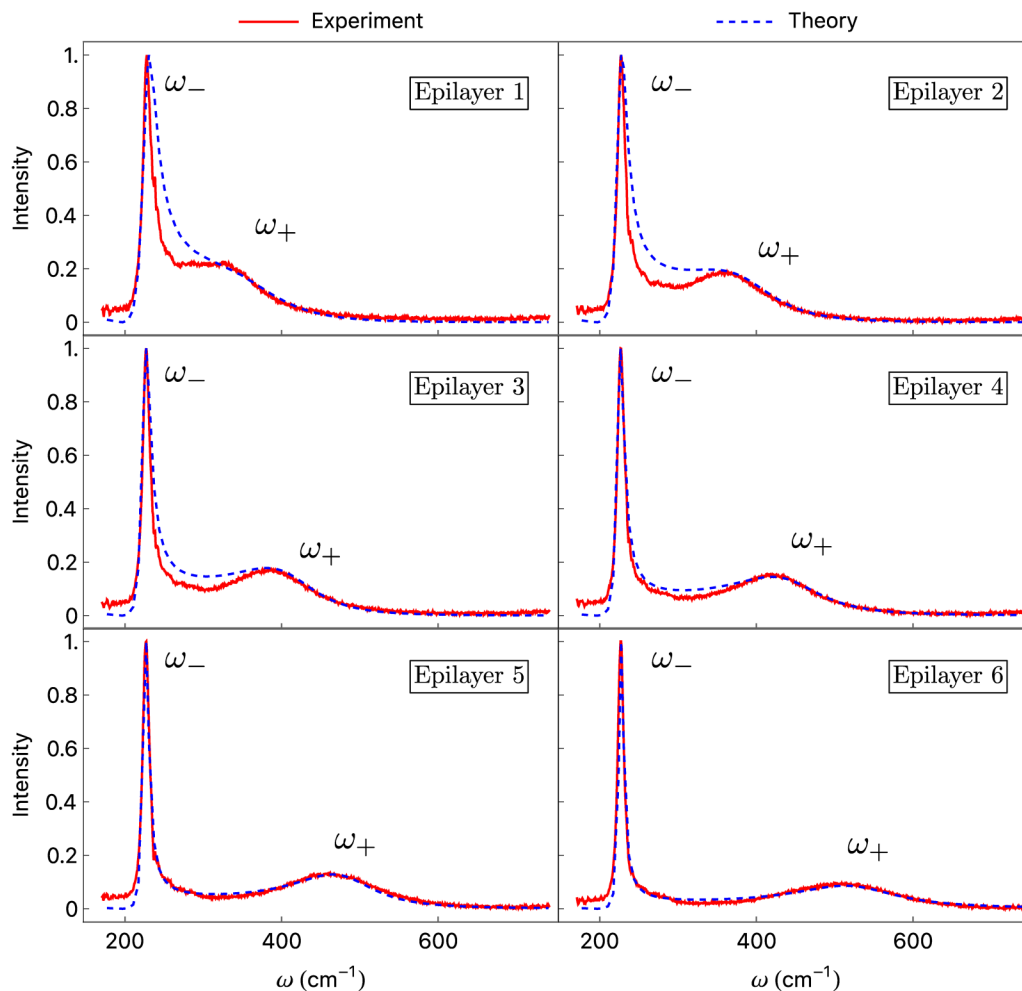


FIG. 2. Raman spectra of GaSb samples with different carrier concentrations. Solid lines are measured spectra and dashed lines are theoretical fits based on the (NP-E) model. ω_- and ω_+ indicate correspondingly the low- and high-frequency coupled phonon-plasmon modes.

Downloaded from http://pubs.aip.org/jap/article-pdf/doi/10.1063/5.0140357/16883988/155702_1_5.0140357.pdf

for the ellipsoidal form of the L -band, we observe a significant difference in the electron carrier density in the L -band, n_L . We note in Fig. 1(b) that this difference in n_L persists even at low doping densities for which the Fermi energies tend to be near the top of the valence band. This result indicates that an isotropic approximation to the L -band in terms of the geometric mean of the longitudinal and transverse effective masses, $m_L = (m_{ll}^2 m_{\perp l})^{1/3}$, underestimates the electron density in the L -band at room temperature. This also suggests that the low-temperature approximation to the electron density in ellipsoidal energy bands, consisting of replacing the Fermi by the Boltzmann distribution (see, e.g., Ref. 55) in the expression for the electron density, may fail already at room temperature for GaSb. However, we note in Appendix D and Fig. 6 that an isotropic parabolic model can approximate the density-of-states for the L -band with an effective mass of about 1.7 times the geometric mean.

We show the Raman spectra for the six epilayers in Fig. 2 and the theoretical line shapes obtained from the (NP-E) model. The line shapes from this model are in excellent agreement with the measured data. Qualitatively, the quality of fits from all three models were comparable. However, the (P-P) model could not reproduce the relative intensities of the coupled mode spectra without changing the Faust-Henry coefficient from -0.21 for the epilayer 1 spectrum to -0.245 for the epilayer 6 spectrum. (The Faust-Henry coefficient was constant for the other two models.) Quantitatively, the different models resulted in different Fermi energies and total carrier concentrations for a given epilayer. The (P-P), the (NP-P), and the (NP-E) model produced the largest, an intermediate, and the smallest Fermi energy, respectively, for a given epilayer. This trend was a consequence of the different density of states for a given energy increment for each model. Including the nonparabolicity of the Γ -minimum results in an increased density of states in this minimum for the (NP-P) model compared to the (P-P) model. Accounting for the anisotropy of the L -minima with an ellipsoidal model rather than a spherical approximation results in an increased density of states in this minimum for the (NP-E) model compared to the other two models. With respect to total carrier concentration, the results are shown in Fig. 3 where the n_{tot} obtained from fits to the Raman line shapes are plotted vs the Hall effect carrier concentration (see Table I). The (NP-P), the (P-P), and the (NP-E) model produced the smallest, an intermediate, and the largest values, respectively, for a given epilayer. Hence, the assumption of isotropic L minima in the spectral models consistently results in lower carrier concentrations when compared to the model with ellipsoidal L minima. In comparison with the total carrier concentration obtained from the (P-P) model for each epilayer, the (NP-P) model predicts concentrations 10%–20% smaller, while the estimates from the (NP-E) model are 60%–20% larger for the low- to high-density epilayers. We also note that the susceptibility χ_e^{GaSb} in Eq. (5) for the (NP-E) model depends on the relative angle between the scattering wavevector \vec{q} and the longitudinal direction in the L -band minima, \vec{k}_L . We report the results for the fits using the (NP-E) model in Table III.

Each model provides different values for electron density. It is difficult to evaluate the accuracy of each model given the complexity of the GaSb band structure. Raman spectral models are often

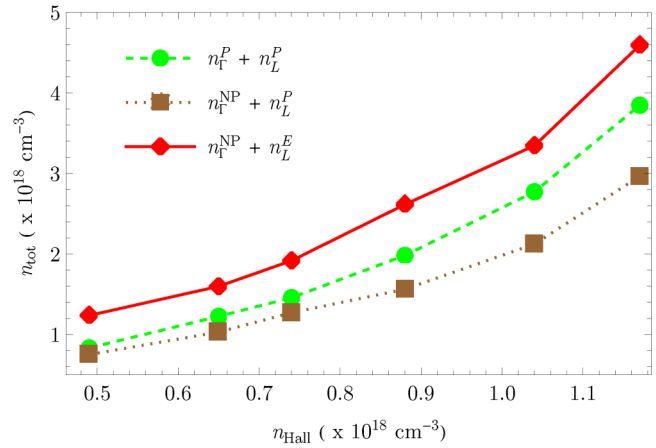


FIG. 3. n_{tot} vs n_{Hall} for the three GaSb band-structure models. (green dots—dashed line) (P-P) model, (brown squares—dotted line) (NP-P) model, and (red diamonds—solid line) (NP-E) model.

validated by comparison to Hall effect measurements. However, such comparisons for most III-V compounds involve a single carrier type in an isotropic energy band minimum, which is not the case for GaSb. Therefore, we assess the quality of each model by calculating the electron mobility ratio, $\mu_r = \mu_L/\mu_\Gamma$, from the relation between the Γ and L -minima in the spectral models and from the Hall effect electron density measurements n_{Hall} . We use the following expression⁵⁶ to accomplish this:

$$n_{\text{Hall}} = \frac{(n_\Gamma + n_L \mu_r)^2}{n_\Gamma + F(K_L) n_L \mu_r^2}, \quad (20a)$$

or, equivalently,

$$\mu_r = \frac{-n_\Gamma n_L + \sqrt{n_\Gamma n_L n_{\text{Hall}} [n_L - F(K_L)(n_\Gamma - n_{\text{Hall}})]}}{n_L^2 - n_{\text{Hall}} F(K_L) n_L}, \quad (20b)$$

where $F(K_L)$ is the anisotropy factor of the L minimum given by

$$F(K_L) = \frac{3K_L(K_L + 2)}{(2K_L + 1)^2}, \quad (21)$$

TABLE III. Fermi energy, damping parameters, and electron densities from the Raman spectral fits for the (NP-E) model.

Epilayer	E_F (eV)	γ_Γ (meV)	γ_L (meV)	$n_\Gamma \times 10^{18}$ (cm ⁻³)	$n_L \times 10^{18}$ (cm ⁻³)	$n_{\text{tot}} \times 10^{18}$ (cm ⁻³)
1	0.008	0.1	0.4	0.160	1.075	1.236
2	0.015	0.2	0.87	0.195	1.402	1.598
3	0.020	0.4	3.2	0.224	1.693	1.917
4	0.029	1.5	5.4	0.279	2.336	2.615
5	0.036	2.0	10	0.329	3.017	3.345
6	0.045	3.1	24.8	0.402	4.191	4.593

Downloaded from http://pubs.aip.org/jap/article-pdf/doi/10.1063/5.0140357/16883988/155702_1_5.0140357.pdf

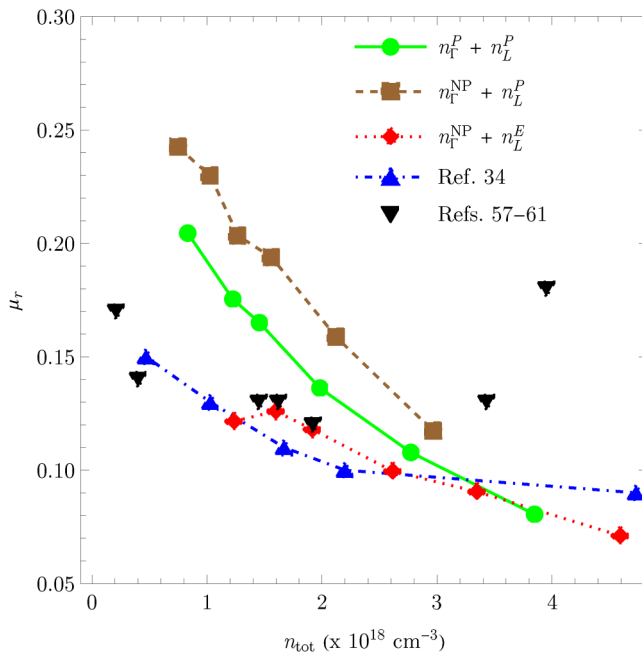


FIG. 4. Mobility ratio μ_r predicted from the carrier concentrations obtained from fits to the Raman line shapes and the three band-structure models. The reference values in blue are taken from Ref. 34, and those in black are taken from Refs. 57–61.

with $K_L = m_{IL}/m_{LL}$. Equation (20) assumes that the Hall scattering factors are equal to unity. We compare the predicted μ_r values with those reported in Ref. 34 in Fig. 4. Indeed, the (NP-E) model is in better agreement with the experimental mobility-ratio measurements than the other two models.

We note the following two assumptions. First, the foregoing three models do not include the many-body effects due to possible high carrier densities, such as those associated with exchange and correlation energies. These effects lead to distorted-perturbed densities of states and changes in separations among the various conduction and valence subbands,^{42,62} and second, the foregoing three models depend only on the separation between the energy levels of the conduction Γ subband and L subband minima. Reports on this dependence^{63,64} suggest that the energy spacing does not decrease by more than $\sim 10\%$ over the total carrier concentration range of 10^{17} cm^{-3} to 10^{18} cm^{-3} . Because we achieved without including the many-body effect agreement with mobility ratios needed to reproduce Hall electron densities, we speculate that the variation with electron density of the separation between the Γ subband and L subband minima energy is not quantitatively significant for extracting electron densities from Raman spectra of GaSb.

V. CONCLUSION

We have demonstrated that a Lindhard–Mermin optical susceptibility model with contributions from carriers in the two lowest GaSb conduction-band minima can be used to simulate coupled

phonon–plasmon mode Raman spectra in n -type GaSb. We investigated the impact on the spectral simulations of three conduction-band models in the optical susceptibility expression. The three conduction-band models were (1) both minima parabolic and isotropic, (2) the Γ minimum non-parabolic and isotropic and the L minima parabolic and isotropic, and (3) the Γ minimum non-parabolic and isotropic and the L minima parabolic and ellipsoidal. For a given epilayer, the carrier concentrations were consistently higher for the model with the ellipsoidal L minima compared to the other two models with isotropic L minima. To evaluate the conduction-band models, we calculated the electron mobility ratio necessary for the electron concentrations from the Raman spectral measurements to reproduce those from the Hall effect measurements. The model with the ellipsoidal L minima agreed best with reported carrier-dependent mobility-ratio values. Hence, it is likely that the total carrier concentration will be underestimated when isotropic L minima in GaSb conduction-band models are assumed, at least at room temperature and for higher doping levels. This observation could have implications not only for Raman spectral modeling but also for any investigation involving the GaSb conduction-band structure.

ACKNOWLEDGMENTS

The authors acknowledge many discussions with their colleagues at the National Institute of Standards and Technology, especially Garnett Bryant and David G. Seiler. The authors gratefully acknowledge C. A. Wang for supplying the epilayers and D. A. Shiao for performing the single magnetic field Hall effect measurements.

Certain commercial equipment, instruments, or materials are identified in this paper in order to specify the experimental procedure adequately. Such identification is not intended to imply recommendation or endorsement by the National Institute of Standards and Technology, University of Maryland, and AltaTech Strategies LLC, nor is it intended to imply that the materials or equipment identified are necessarily the best available for the purpose.

AUTHOR DECLARATIONS

Conflict of Interest

The authors have no conflicts to disclose.

Author Contributions

Maicol A. Ochoa: Conceptualization (equal); Formal analysis (equal); Investigation (equal); Methodology (equal); Software (equal); Writing – original draft (equal); Writing – review & editing (equal). **James E. Maslar:** Conceptualization (equal); Data curation (equal); Formal analysis (equal); Investigation (equal); Methodology (equal); Project administration (equal); Supervision (equal); Writing – review & editing (equal). **Herbert S. Bennett:** Conceptualization (equal); Formal analysis (equal); Investigation (equal); Methodology (equal); Project administration (equal); Supervision (equal); Writing – review & editing (equal).

DATA AVAILABILITY

The data that support the findings of this study are available from the corresponding author upon reasonable request.

APPENDIX A: LINE SHAPE

We obtained the coupled mode spectra by subtracting contributions corresponding to LO phonon Raman scattering, second order phonon scattering, nitrogen and oxygen scattering from ambient air, and a cubic polynomial baseline from the original spectra. We simulated the LO phonon contribution by fitting separate Gaussian functions to each side of the LO phonon peak at 236.21 cm^{-1} (the LO phonon was asymmetric) and by subtracting the resulting fit from the measured spectrum. For simplicity, the line shapes were fit with a single functional form. A Gaussian line shape was selected rather than a Lorentzian line shape as the former provided a better fit to the observed features (the instrument function presumably dominated the observed line shape).

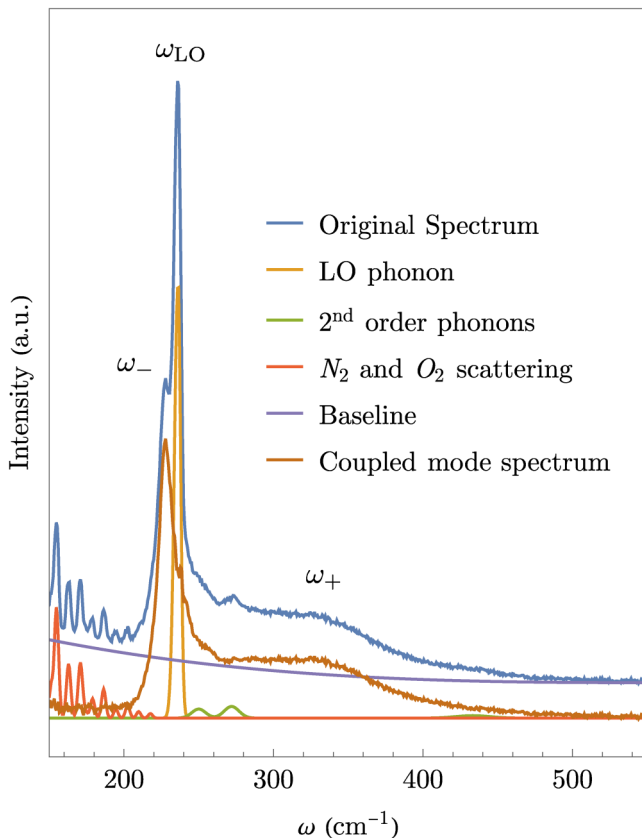


FIG. 5. The coupled phonon–plasmon mode spectrum of Epilayer 1 is obtained by subtracting contributions from LO phonon Raman scattering, second order phonon Raman scattering, N_2 and O_2 molecular Raman scattering, and a cubic polynomial baseline from the original spectrum. ω_- denotes the low-frequency coupled phonon–plasmon mode; ω_{LO} , the LO phonon mode, and ω_+ , the high-frequency coupled phonon–plasmon mode.

Except for the peak amplitude, all respective peak parameters were constant for all spectra. The peak amplitude was decreased as the doping level increased, and the width of the surface space charge region decreased.⁴⁸ We simulated the second order Raman scattering features⁶⁵ with Gaussian peaks centered at 250, 272, and 433.3 cm^{-1} . The respective peak parameters were constant for all spectra and were determined from fits to the measured data in spectra where the respective features could best be spectrally resolved from any phonon–plasmon modes. We simulated the scattering from nitrogen and oxygen molecules in ambient air with Gaussian peaks. The respective peak parameters were constant for all spectra and were determined from fits to the measured data. We simulated the non-linear background using a cubic polynomial expression that was identical for all spectra except for the constant term. An example of the removal of these features from the original Epilayer 1 spectrum to obtain the coupled mode spectrum is shown in Fig. 5.

APPENDIX B: GaSb PARAMETERS

In this Appendix, we obtain the bandgap energies, effective masses, and a Γ -band nonparabolicity factor used in our band-structure models reported in Table II. We include the parameters used in these calculations in Table IV.

1. *Bandgap energies.* The bandgap energies were calculated assuming that the band minimum temperature dependence can be expressed in the Varshni form,

$$E_i(T) = E_i(T=0) - \frac{\alpha_i T^2}{T + \beta_i}. \quad (\text{B1})$$

These values for the Varshni parameters result in $E_{\text{LO}} - E_{\Gamma 0} = 0.0847 \text{ eV}$, which lies near the median of the range

TABLE IV. Parameter values used in the computation of the bandgap energies, effective masses, and a Γ -band nonparabolicity factor, as described in Appendix B.

Parameter	Value	Parameter	Value
Bandgap energies^a			
$E_{\Gamma}(0\text{K})$	0.813 eV	$E_L(T=0)$	0.902 eV
α_{Γ}	$3.78 \times 10^{-4} \text{ eV/K}$	α_L	$3.97 \times 10^{-4} \text{ eV/K}$
β_{Γ}	94 K	β_L	94 K
Effective masses			
$m_{\Gamma}(0 \text{ K})^{\text{b}}$	$0.039 m_o$	$m_{\text{tL}}(0\text{K})^{\text{c}}$	$0.085 m_o$
		$E_1(10 \text{ K})^{\text{d}}$	2.184 eV
$\Delta_{\text{SO}}^{\text{b,e}}$	0.76 eV	$\Delta_1(10\text{K})^{\text{d,e}}$	0.435 eV
E_p^{f}	7.96 eV	E_p^{f}	12.82 eV
		$E_1(300 \text{ K})^{\text{d}}$	2.184 eV
		$\Delta_1(300 \text{ K})$	0.442 eV

^aReference 47.

^bReference 66.

^cReference 51.

^dReference 70.

^eAssumed T -independent.

of reported values, which is 0.040–0.120 eV.^{66–68} For $E_{L0}-E_{\Gamma 0}$ values of 0.040 eV and 0.120 eV, the n_{tot} values obtained from fits to the spectra were $7.82 \times 10^{18} \text{ cm}^{-3}$ and $2.27 \times 10^{18} \text{ cm}^{-3}$, respectively. This n_{tot} range corresponds to $4.593 \times 10^{18} \text{ cm}^{-3} + 70\% / - 51\%$ (the n_{tot} value obtained for $E_{L0}-E_{\Gamma 0} = 0.0847 \text{ eV}$). While the n_{tot} value depends on the choice of the $E_{L0}-E_{\Gamma 0}$ value, it is beyond the scope of this work to definitively identify the $E_{L0}-E_{\Gamma 0}$ value.

2. The Γ minimum effective mass. The temperature-dependent band edge Γ effective mass, $m_{\Gamma}(T)$, was calculated from Ref. 69,

$$\frac{m_o}{m_{\Gamma}(T)} = 1 + E_p^{\Gamma} \left(\frac{2}{E_{\Gamma}(T)} + \frac{1}{E_{\Gamma}(T) + \Delta_{\text{SO}}} \right) \quad (\text{B2})$$

3. The L minimum transverse effective mass. The temperature-dependent band edge L transverse effective mass, $m_{\text{tL}}(T)$, was calculated from Ref. 69,

$$\frac{m_o}{m_{\text{tL}}(T)} = 1 + E_p^L \left(\frac{2}{E_1(T)} + \frac{1}{E_1(T) + \Delta_1} \right). \quad (\text{B3})$$

4. The L minimum longitudinal effective mass. The band edge L longitudinal effective mass, m_{L} , is assumed to be temperature-independent.
5. Non-parabolicity factor for Γ minimum. The Γ minimum non-parabolicity factor was calculated from using 300 K values where applicable,⁵²

$$\zeta = \frac{(1 - m_{\Gamma}^{\text{DOS}}/m_o)^2 (3E_{\Gamma}^2 + 4E_{\Gamma}\Delta_{\text{SO}} + 2\Delta_{\text{SO}}^2)}{(E_{\Gamma} + \Delta_{\text{SO}})(3E_{\Gamma} + 2\Delta_{\text{SO}})}. \quad (\text{B4})$$

APPENDIX C: Γ BAND DOS: NONPARABOLIC MODEL

We consider an isotropic dispersion relation near the conduction-band minimum $k_o = 0$,

$$E(k) = E_o + \frac{(\hbar k)^2}{2m} + \left(\frac{\zeta}{E_o} \right) \left(\frac{(\hbar k)^2}{2m} \right)^2, \quad (\text{C1})$$

and calculate the density of states (DOS)

$$\rho(\epsilon) \equiv \int \frac{d^3k}{(2\pi)^3} \delta(\epsilon - E(k)) \quad (\text{C2})$$

by substituting Eq. (C1) into Eq. (C2) and introducing the following variable substitution:

$$u = \frac{(\hbar k)^2}{2m} \quad du = \frac{\hbar^2 k}{m} dk = \frac{\sqrt{2}\hbar}{\sqrt{m}} \sqrt{u} dk. \quad (\text{C3})$$

In this form, the DOS reads

$$\rho(\epsilon) = \frac{1}{4\pi^2} \frac{(2m)^{3/2}}{\hbar^3} \int du \sqrt{u} \delta\left(\epsilon - E_o - u - \left(\frac{\zeta}{E_o}\right) u^2\right). \quad (\text{C4})$$

We define u_{\pm} by

$$u_{\pm} = \frac{-1}{2(\zeta/E_o)} \left(1 \pm \sqrt{1 + 4(\zeta/E_o)(\epsilon - E_o)} \right) \quad (\text{C5})$$

such that

$$\begin{aligned} \delta\left(\epsilon - E_o - u - \left(\frac{\zeta}{E_o}\right) u^2\right) &= \delta(-[\zeta/E_o](u - u_-)(u - u_+)) \\ &= \frac{1}{|\zeta/E_o|} \delta((u - u_-)(u - u_+)) \\ &= \frac{\delta(u - u_+) + \delta(u - u_-)}{|\zeta/E_o| |u_- - u_+|}. \end{aligned} \quad (\text{C6})$$

We integrate the expression in Eq. (C4) near the band minimum ($k = 0$) in the region where the nonparabolic form in Eq. (C1) is physical. Since the root u_+ diverges as ζ vanishes, this root is unphysical and falls out of the integration range. We conclude that

$$\rho(\epsilon) = \frac{1}{4\pi^2} \frac{(2m)^{3/2}}{\hbar^3} \frac{1}{|\zeta/E_o| |u_- - u_+|} [\sqrt{u_-}] \quad (\text{C7})$$

$$= \frac{1}{4\pi^2} \frac{(2m)^{3/2}}{\hbar^3} \frac{\sqrt{1 - \sqrt{1 + 4(\zeta/E_o)(\epsilon - E_o)}}}{\sqrt{-2(\zeta/E_o)} \sqrt{1 + 4(\zeta/E_o)(\epsilon - E_o)}}. \quad (\text{C8})$$

Finally, utilizing $\sqrt{1+x} \approx 1 + \frac{1}{2}x$ when $x \ll 1$, we note that $\rho(\epsilon) \rightarrow \frac{1}{4\pi^2} \frac{(2m)^{3/2}}{\hbar^3} \sqrt{\epsilon - E_o}$ when $\zeta \rightarrow 0$.

APPENDIX D: L -BAND DOS: ELLIPSOIDAL MODEL

We adopt an ellipsoidal model for the L -band structure near each one of their corresponding minima,

$$E(k) = E_o + \frac{(\hbar k_x)^2}{2m_{\text{L}}} + \frac{\hbar^2}{2m_{\text{L}}} (k_x^2 + k_y^2). \quad (\text{D1})$$

We find the L -band DOS by substituting Eq. (D1) into Eq. (C2) and integrating in \mathbf{k} -space after changing variables to prolate spherical ellipsoidal coordinates (μ, ν, ϕ) ,

$$k_x = a \sinh \mu \sin \nu \cos \phi, \quad (\text{D2})$$

$$k_y = a \sinh \mu \sin \nu \sin \phi, \quad (\text{D3})$$

$$k_z = a \cosh \mu \cos \nu, \quad (\text{D4})$$

with $\mu > 0$, $\nu \in (0, \pi)$, and $\phi \in (0, 2\pi)$. a is a length parameter that depends on the ellipsoids in Eq. (D1) and that we obtain in Eq. (D7). In the prolate coordinate system, the volume of integration d^3k

$$d^3k = a^3 \sinh \mu \sin \nu (\sinh^2 \mu + \sin^2 \nu) d\mu d\nu d\phi. \quad (\text{D5})$$

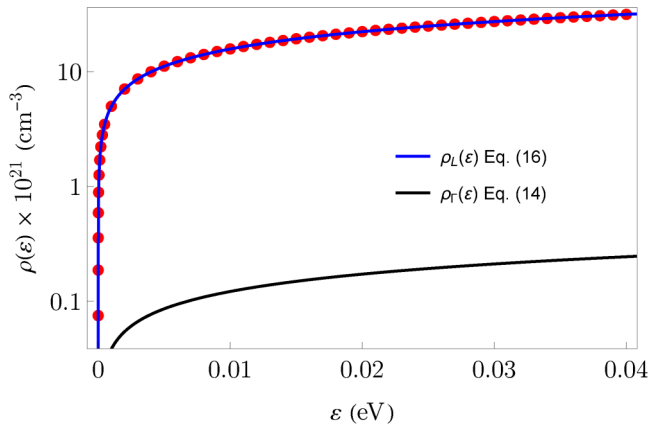


FIG. 6. Density of states for the bands in the (NP-E) model. We show the *L*-band DOS in Eq. (16) (dotted—red) vs a parabolic model with $m_{\text{eff}} = 0.8957$ and $N_{\text{eq}} = 1$ (solid—blue), and the nonparabolic Γ -band DOS in Eq. (14) (solid—black).

Writing Eq. (D1) in the form

$$1 = \frac{k_z^2}{2m_{\text{IL}}(E(k) - E_0)/\hbar^2} + \frac{k_x^2 + k_y^2}{2m_{\text{IL}}(E(k) - E_0)/\hbar^2} \quad (\text{D6})$$

and considering that $m_{\text{IL}} > m_{\text{L}}$, we find a ,

$$a = \frac{2(E(k) - E_0)\sqrt{m_{\text{L}}^2 - m_{\text{IL}}^2}}{\hbar^2}. \quad (\text{D7})$$

After integration with respect to μ and ϕ , we obtain the DOS reported in Eq. (16). Figure 6 presents the GaSb ρ_L as a function of energy $E - E_{L0}$. Note that *L*-band DOS can be fit to the DOS corresponding to the parabolic band, with an effective mass approximately equal to $1.7(m_{\text{L}}^2 m_{\text{IL}})^{1/3}$.

APPENDIX E: ELECTRON DENSITY FITTING FUNCTIONS

The *L*-band electron carrier concentration $n_L(E_F)$ at room temperature and as a function of E_F is given by

$$n_L(E_F) = 4 \int d\epsilon \rho_L(\epsilon) f(\epsilon - E_F), \quad (\text{E1})$$

TABLE V. Fitting parameters for the polynomial approximation to the electron density in Eq. (E2) at 300 K.

Coeff.	n_L	n_Γ
a_0	8.06674×10^{17}	1.2643×10^{17}
a_1	2.93115×10^{19}	3.89395×10^{18}
a_2	5.19088×10^{20}	4.67419×10^{19}
a_3	8.21191×10^{21}	1.53756×10^{20}
a_4	8.2598×10^{22}	-1.05847×10^{21}

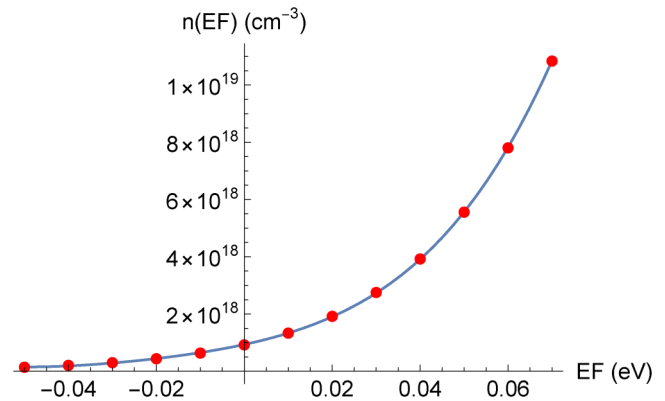


FIG. 7. Comparison between the exact (dots—red) and approximate (solid—blue) total electron density at 300 K as a function of the Fermi energy.

where $f(E - E_F)$ is the Fermi distribution function, which we can evaluate numerically. Here, we provide a polynomial approximation as a function of E_F of the form

$$n_L(E_F) \approx \sum_{i=0}^4 a_i E_F^i, \quad (\text{E2})$$

considering also an identical approximation to $n_\Gamma(E_F)$. Table V reports the fitting parameters a_i for the (NP-E) model at 300 K (Fig. 7).

REFERENCES

- T. D. Eales, I. P. Marko, A. R. Adams, J. R. Meyer, I. Vurgaftman, and S. J. Sweeney, *J. Phys. D: Appl. Phys.* **54**, 055105 (2021).
- A. Ikyo, I. Marko, K. Hild, A. Adams, S. Arafat, M.-C. Amann, and S. Sweeney, *Sci. Rep.* **6**, 19595 (2016).
- F. A. Al-Saymari, A. P. Craig, Q. Lu, A. R. Marshall, P. J. Carrington, and A. Krier, *Opt. Express* **28**, 23338 (2020).
- L. Monge-Bartolome, B. Shi, B. Lai, G. Boissier, L. Cerutti, J.-B. Rodriguez, K. M. Lau, and E. Tournié, *Opt. Express* **29**, 11268 (2021).
- E. Tournié, L. Monge Bartolome, M. Rio Calvo, Z. Loghmani, D. A. Diaz-Thomas, R. Teissier, A. N. Baranov, L. Cerutti, and J.-B. Rodriguez, *Light Sci. Appl.* **11**, 1 (2022).
- W. Huang, L. Li, L. Lei, J. A. Massengale, R. Q. Yang, T. D. Mishima, and M. B. Santos, *J. Appl. Phys.* **123**, 113104 (2018).
- F. Rothmayr, E. D. Guarín Castro, F. Hartmann, G. Knebl, A. Schade, S. Höfling, J. Koeth, A. Pfenning, L. Worschech, and V. Lopez-Richard, *Nanomaterials* **12**, 1024 (2022).
- P. C. Klipstein, *Appl. Phys. Lett.* **120**, 060502 (2022).
- E. D. Guarín Castro, F. Rothmayr, S. Krüger, G. Knebl, A. Schade, J. Koeth, L. Worschech, V. Lopez-Richard, G. E. Marques, F. Hartmann, A. Pfenning, and S. Höfling, *AIP Adv.* **10**, 055024 (2020).
- Z.-X. Yang, F. Wang, N. Han, H. Lin, H.-Y. Cheung, M. Fang, S. Yip, T. Hung, C.-Y. Wong, and J. C. Ho, *ACS Appl. Mater. Interfaces* **5**, 10946 (2013).
- N.-T. Yeh, P.-C. Chiu, J.-I. Chyi, F. Ren, and S. J. Pearton, *J. Mater. Chem. C* **1**, 4616 (2013).
- D. Benyahia, Ł. Kubiszyn, K. Michalczewski, A. Keblowski, P. Martyniuk, J. Piotrowski, and A. Rogalski, *J. Electron. Mater.* **47**, 299 (2018).

- ¹³Q. Lu, A. Marshall, and A. Krier, *Materials* **12**, 1743 (2019).
- ¹⁴C. L. Canedy, W. W. Bewley, S. Tomasulo, C. S. Kim, C. D. Merritt, I. Vurgaftman, J. R. Meyer, M. Kim, T. J. Rotter, G. Balakrishnan, and T. D. Golding, *Opt. Express* **29**, 35426 (2021).
- ¹⁵W. Beck and J. Anderson, *J. Appl. Phys.* **62**, 541 (1987).
- ¹⁶F. Zhang, J. F. Castaneda, T. H. Gfroerer, D. Friedman, Y.-H. Zhang, M. W. Wanlass, and Y. Zhang, *Light Sci. Appl.* **11**, 1 (2022).
- ¹⁷J. Geurts, *Phys. Status Solidi B* **252**, 19 (2015).
- ¹⁸G. Abstreiter, M. Cardona, and A. Pinczuk, "Light scattering by free carrier excitations in semiconductors," in *Light Scattering in Solids IV: Electronics Scattering, Spin Effects, SERS, and Morphic Effects*, edited by M. Cardona and G. Güntherodt (Springer, Berlin, 1984), pp. 5–150.
- ¹⁹G. Abstreiter, E. Bauser, A. Fischer, and K. Ploog, *Appl. Phys.* **16**, 345 (1978).
- ²⁰G. Abstreiter, R. Trommer, M. Cardona, and A. Pinczuk, *Solid State Commun.* **30**, 703 (1979).
- ²¹L. Artús, R. Cuscó, J. Ibáñez, N. Blanco, and G. González-Díaz, *Phys. Rev. B* **60**, 5456 (1999).
- ²²S. Ernst, A. Goni, K. Syassen, and M. Cardona, *Phys. Rev. B* **53**, 1287 (1996).
- ²³U. Nowak, W. Richter, and G. Sachs, *Phys. Status Solidi B* **108**, 131 (1981).
- ²⁴A. Pinczuk, G. Abstreiter, R. Trommer, and M. Cardona, *Solid State Commun.* **21**, 959 (1977).
- ²⁵M. Ramsteiner, J. Wagner, P. Hiesinger, K. Köhler, and U. Rössler, *J. Appl. Phys.* **73**, 5023 (1993).
- ²⁶G. Schwartz, G. Gualtieri, L. Dubois, W. Bonner, and A. Ballman, *J. Electrochem. Soc.* **131**, 1716 (1984).
- ²⁷J. E. Maslar, W. S. Hurst, and C. Wang, *J. Appl. Phys.* **104**, 103521 (2008).
- ²⁸R. Cuscó, J. Ibáñez, and L. Artús, *Appl. Phys. Lett.* **97**, 091909 (2010).
- ²⁹R. Cuscó, E. Alarcón-Lladó, L. Artús, W. S. Hurst, and J. E. Maslar, *Phys. Rev. B* **81**, 195212 (2010).
- ³⁰J. Maslar, W. Hurst, and C. Wang, *J. Appl. Phys.* **106**, 123502 (2009).
- ³¹G. Hu and R. O'Connell, *Phys. Rev. B* **40**, 3600 (1989).
- ³²J. Ibáñez, R. Cuscó, and L. Artús, *Phys. Status Solidi B* **223**, 715 (2001).
- ³³M. A. Ochoa, J. E. Maslar, and H. S. Bennett, *J. Appl. Phys.* **128**, 075703 (2020).
- ³⁴H. Harland and J. Woolley, *Can. J. Phys.* **44**, 2715 (1966).
- ³⁵D. Seiler and W. Becker, *Phys. Lett. A* **26**, 96 (1967).
- ³⁶Y. Livneh, P. Klipstein, O. Klin, N. Snapi, S. Grossman, A. Glozman, and E. Weiss, *Phys. Rev. B* **86**, 235311 (2012).
- ³⁷D. Seiler and W. Becker, *Phys. Rev.* **186**, 784 (1969).
- ³⁸D. Seiler, W. Becker, and L. M. Roth, *Phys. Rev. B* **1**, 764 (1970).
- ³⁹H. J. Lee and J. C. Woolley, *Can. J. Phys.* **59**, 1844 (1981).
- ⁴⁰G. P. Williams, F. Cerrina, G. Lapeyre, J. Anderson, R. Smith, and J. Hermanson, *Phys. Rev. B* **34**, 5548 (1986).
- ⁴¹Z. Ahangari and M. Fathipour, *J. Comput. Electron.* **13**, 375 (2014).
- ⁴²A. Sawamura, J. Otsuka, T. Kato, and T. Kotani, *J. Appl. Phys.* **121**, 235704 (2017).
- ⁴³J. Mudd, N. Kybert, W. Linhart, L. Buckle, T. Ashley, P. King, T. Jones, M. Ashwin, and T. Veal, *Appl. Phys. Lett.* **103**, 042110 (2013).
- ⁴⁴C. Wang, S. Salim, K. Jensen, and A. Jones, *J. Cryst. Growth* **170**, 55 (1997).
- ⁴⁵C. Wang, D. Shiao, R. Huang, C. Harris, and M. Connors, *J. Cryst. Growth* **261**, 379 (2004).
- ⁴⁶R. Baxter, F. Reid, and A. Beer, *Phys. Rev.* **162**, 718 (1967).
- ⁴⁷M. Levinstein, *Handbook Series on Semiconductor Parameters* (World Scientific, 1997), Vol. 1, pp. 125–146.
- ⁴⁸J. Maslar, W. Hurst, and C. A. Wang, *Appl. Spectrosc.* **61**, 1093 (2007).
- ⁴⁹M. V. Klein, B. N. Ganguly, and Priscilla J. Colwell, *Phys. Rev. B* **6**, 2380 (1972).
- ⁵⁰N. D. Mermin, *Phys. Rev. B* **1**, 2362 (1970).
- ⁵¹H. Arimoto, N. Miura, R. Nicholas, N. Mason, and P. Walker, *Phys. Rev. B* **58**, 4560 (1998).
- ⁵²J. Blakemore, *J. Appl. Phys.* **53**, R123 (1982).
- ⁵³M. Hass and B. Hennis, *J. Phys. Chem. Solids* **23**, 1099 (1962).
- ⁵⁴M. Muñoz, K. Wei, F. H. Pollak, J. Freeouf, and G. Charache, *Phys. Rev. B* **60**, 8105 (1999).
- ⁵⁵M. Balkanski, R. F. Wallis, and R. F. Wallis, *Semiconductor Physics and Applications* (Oxford University Press, 2000), Vol. 8, Chap. 6.
- ⁵⁶P. Mathur, N. Kataria, and S. Jain, *J. Phys. Chem. Solids* **39**, 403 (1978).
- ⁵⁷A. Sagar, *Phys. Rev.* **117**, 93 (1960).
- ⁵⁸J. Basinski, S. Rosenbaum, S. Basinski, and J. Woolley, *J. Phys. C: Solid State Phys.* **6**, 422 (1973).
- ⁵⁹J. Basinski, C. C. Kwan, and J. C. Woolley, *Can. J. Phys.* **50**, 1068 (1972).
- ⁶⁰G. Bordure, F. Guastavino, and C. Llinares, *Phys. Status Solidi B* **34**, 759 (1969).
- ⁶¹C. Liang, *J. Appl. Phys.* **39**, 3866 (1968).
- ⁶²F. Bertazzi, A. Tibaldi, M. Goano, J. A. G. Montoya, and E. Bellotti, *Phys. Rev. Appl.* **14**, 014083 (2020).
- ⁶³M. J. Aubin, M. B. Thomas, E. H. V. Tongerloo, and J. C. Woolley, *Can. J. Phys.* **47**, 631 (1969).
- ⁶⁴P. Paskov, *Europhys. Lett.* **20**, 143 (1992).
- ⁶⁵T. Sekine, K. Uchinokura, and E. Matsuura, *Solid State Commun.* **18**, 1337 (1976).
- ⁶⁶I. Vurgaftman, J. Meyer, and L. Ram-Mohan, *J. Appl. Phys.* **89**, 5815 (2001).
- ⁶⁷C. Kourkoutas, P. Bekris, G. Papaioannou, and P. Euthymiou, *Solid State Commun.* **49**, 1071 (1984).
- ⁶⁸A. Walton and S. Metcalfe, *J. Phys. C: Solid State Phys.* **9**, 3855 (1976).
- ⁶⁹D. Aspnes, *Phys. Rev. B* **14**, 5331 (1976).
- ⁷⁰S. Zollner, M. Garriga, J. Humlek, S. Gopalan, and M. Cardona, *Phys. Rev. B* **43**, 4349 (1991).